Fibers and Polymers 2021, Vol.22, No.3, 597-611
DOI 10.1007/s12221-021-0206-8

ISSN 1229-9197 (print version)
ISSN 1875-0052 (electronic version)

Reactive Radical Species in Photocatalytic Activities of PET-Ag-TiO_2 Nanoparticles Composites Under Visible Light Irradiation

Hui Zhang[1†*], Dou Wang[1†], Cuihong Sheng[1], Deping Ben[1], Hailiang Wu[1], and Ningtao Mao[2]

[1]*Research Centre for Functional Textile Materials, School of Textile Science and Engineering,*
Xi'an Polytechnic University, Xi'an 710048, China
[2]*School of Design, University of Leeds, Leeds, LS2 9JT, United Kingdom*

(Received February 24, 2020; Revised May 2, 2020; Accepted June 4, 2020)

Abstract: In this research, the reactive radical species in photocatalytic activities of a composite photocatalyst made from PET filaments loaded with Ag-TiO_2 nanoparticles under visible light irradiation, in comparison with those of as-modified Ag-TiO_2 nanoparticles, were reported and its photocatalytic mechanism was investigated. The PET filaments were modified by using tetrabutyl titanate as the TiO_2 precursor and silver nitrate as the dopant in a hydrothermal process. The Ag decorated TiO_2 nanoparticles were synthesized and deposited on the surfaces of PET filaments in the hydrothermal process at 120 °C for 180 min. The morphology, phase structure, chemical binding state, and optical properties of the PET-Ag-TiO_2 nanoparticles composites were systemically studied by means of field emission scanning electron microscopy (FESEM), X-ray diffraction (XRD), transmission electron microscopy (TEM), X-ray photoelectron spectroscopy (XPS), photoluminescence (PL) spectroscopy, diffuse reflectance spectroscopy (DRS), and ultraviolet photoelectron spectroscopy (UPS) techniques. The photocatalytic activities of the PET-Ag-TiO_2 nanoparticles composites were evaluated in the photodegradation of both methylene blue (MB) and methyl orange (MO) dyes under visible light irradiation. It was found that, unlike in the as-obtained TiO_2 nanoparticles and Ag decorated TiO_2 nanoparticles, the photoinduced holes (h^+) were the major reactive radical species in both PET-Ag-TiO_2 composite photocatalyst and the PET filaments loaded with TiO_2 nanoparticles in the MB photodegradation process. The experimental results also indicated that the PET-Ag-TiO_2 nanoparticles composites led to the improvement of the separation efficiency of photogenerated electron-hole pairs. The enhanced photocatalytic activity of the PET filaments coated with Ag decorated TiO_2 nanoparticles was ascribed to both the incorporation of Ag nanoparticles into TiO_2 nanoparticles and the possible infiltration of Ag/Ti nanoparticles into PET polymers. In addition, the wavelength and intensity of monochromatic light had great influences on the photodegradation rate of dye used, which was closely correlated with the maximum absorption wavelength of the dye to be degraded.

Keywords: Ag nanoparticle decorated TiO_2, PET filament, Photocatalytic activity, Visible light

Introduction

Titanium oxide (TiO_2) has been extensively used in a wide range of fields such as coating, cosmetics, papermaking, chemical fiber, rubber, optoelectronics, and photocatalysis. As one of the semiconductor-based photocatalysts, it can decompose a broad scope of organic pollutants by photo-oxidation reaction because of its low cost, low toxicity, superior optical and electronic properties, and high chemical stability [1]. These organic pollutants like methylene blue (MB) and methyl orange (MO) dyes remained in the textile industry effluents are difficult to degrade by conventional wastewater treatment techniques and would cause serious impacts on the environment [2]. However, the photocatalytic activity of TiO_2 has been greatly restrained mainly due to the relatively wide band gap and the low photo-induced charge carrier separation efficiency [3]. These shortcomings can be overcome by modification in electronic band structure of TiO_2 to suppress the recombination rate of electron-hole pairs [4]. To date different strategies like facet engineering [5], morphology and size controlling [6], and electronic band matching [7] techniques have been developed to exploit the visible-light-deriven TiO_2 based photocatalysts. Enormous efforts have been devoted to modify the structure and composition of TiO_2 to enhance its photocatalytic properties under visible light illumination. For instance, the presence of defects/dopants or the particle size can tune the electronic properties of TiO_2 [8]. The introduction of polyoxometalate species not only enhances the light adsorption and redox activity of TiO_2, but also improves the photochemical stability of plasmonic TiO_2 composites owing to the relatively narrow band gap and low reversible redox potential of polyoxoanion [9]. The synergistic effect of bi-plasmonic Au-Ag alloyed nanoparticles is applied for preparation of Au-Ag@TiO_2@Fe_3O_4 nanoparticles for degradation of rhodamine-6G dye [10].

Recent results have shown that the optical properties of TiO_2 are influenced by a variety of dopants, such as nonmetal elements of N, C, and S [11], transition metals of Fe, Co, Ni, Cu [12], and noble metals of Pt, Pd, Ag [13], due to the electronic rearrangement, electron transfer at the surface, and photo-induced conductivity, which result in an efficient increase in light absorption especially in visible light waveband [14]. The enhanced light absorption leads to the superior photocatalytic activity of doped TiO_2, which can be

---

*Corresponding author: hzhangw532@xpu.edu.cn
†These authors contribute equally to this work.

employed as photocatalysis for decomposition of dyeing effluents. Upon light illumination, the electron-hole pairs are first generated from TiO_2, and thus producing ·OH radicals. These active radicals take part in the photo-degradation of dyes following the Eley-Rideal mechanism [15].

There have been considerable efforts to functionalize the surface of metal oxide semiconductors with plasmonic nanoparticles in order to overcome the limiting factors identified for photocatalysis. It is demonstrated that the small Au nanoparticles exhibit the enhanced surface plasmon resonance (SPR) effect and the big Au nanoparticles act as the electron transfer center, which affects the photocatalytic activity of g-C_3N_4/BiOBr under visible light irradiation [16]. The crystallite size of anatase TiO_2 is reduced after being co-modified with Ag/Ce^{4+}/La^{3+} and its higher degradation efficiency is ascribed to the synergistic effect of Ce^{4+}/La^{3+} and Ag^0 [17].

Compared with other noble metals of Au and Pt, more recent work on the modification of TiO_2 is focused on the doping of Ag because of its antibacterial activity and low cost [18]. The electrons are accumulated in Ag core of Ag@TiO_2 nanoparticle until the Fermi level equilibrium is achieved, while the electrons get discharged when an electron acceptor like O_2 is introduced into the reaction system [19]. Many Ag modified TiO_2 triple-component photocatalysts have been reported to impart with the higher photocatalytic activity. For example, Ag nanoparticles and reduced graphene oxide (rGO) not only enhance the light harvest, but also increase the capacity of electron accepting from Ag decorated triple-component Ag_3PO_4/TiO_2/rGO composite [20]. Another three-component plasmonic photocatalyst of Ag-TiO_2-C_3N_4 or Au-TiO_2-C_3N_4 under visible light illumination having superior photocatalytic activity has been reported, and it's superior photoactivity is attributed to the synergetic effect of SPR of plasmonic metal nanoparticles, plasmon excitation in the nearest semiconductors, and interfacial separation and transfer of photo-induced electrons and holes [21]. However, it is a major concern to further utilize the particulate photocatalysts because it is hard to recover them from aqueous solutions.

Anchoring of TiO_2 nanoparticles onto textile supports offers an alternative way to obtain the photocatalytic self-cleaning capabilities, UV protection, antimicrobial and bioactive properties [22]. More recently, various methods have been employed to immobilize Ag doped TiO_2 nanocomposites on the surfaces of glass [23], carbon [24], polypropylene [25], chitosan [26], cotton [27] and PVDF@TiO_2 [28] fibers or cotton [29], polyethylene terephthalate (PET)/cotton [30] and cotton/PET [31] fabrics. The photocatalytic activity can be further enhanced *via* calcination to remove the polypyrrole-assisted template [32]. It has been reported that the reactive dyes possess an ability to increase the adsorption and adhesion of Ag/TiO_2 nanocomposite on cotton fabrics [33]. The plasma technique has been applied for polypropylene fiber to introduce polar groups on fiber surface to improve the binding strength between Ag and TiO_2 nanoparticles [34]. Moreover, TiO_2/Ag nanoparticles can also be incorporated into the spun-bonded/melt-blown nonwovens to fabricate the multifunctional air filters [35].

In previous studies, the effects of different parameters such as TiO_2 phase structure [7], pH value and photocatalyst dosage [36], fiber morphology [37], isotherm equilibrium and kinetic behaviors [38], core-shell structure type [16], work function and Fermi level of TiO_2 [39] on the photocatalytic activity of Ag doped TiO_2 have been systematically investigated. Recent experiments have supported that the matching of the irradiation light frequency with the slow-photon energy range on TiO_2 results in a remarked increase of visible light-induced dye photosensitized degradation [4]. The photocatalytic activities of TiO_2 are different under monochromatic visible light and polychromatic simulated sun light irradiation [40]. In addition, the photodegradation efficiency of methyl paraoxon by Ag flakes is affected by the wavelength of incident radiation, which is related with the resonance of plasmonic Ag flakes. More specifically, when the plasmonic resonance of Ag flakes is closely matched with the wavelength of incident radiation, the maximum charge generation and catalytic breakdown of methyl paraoxon can be reached [41]. However, previous studies do not address the formation of reactive radical species on the Ag doped TiO_2 which are loaded on the surface of polymer matrixes.

Herein, the present study explores the mechanism of the formation of reactive species generated by the Ag nanoparticles decorated TiO_2 coated PET filaments under visible light irradiation. In detail, PET filaments were used as the substrate to deposit Ag nanoparticles decorated TiO_2 nanoparticles. The morphology, phase structure, chemical binding state, and optical properties of the as-prepared filaments were characterized by using various techniques. The photocatalytic mechanism of the PET-Ag-TiO_2 nanoparticles composites for photodegradation of MB dye and MO dye under visible light irradiation was revealed. This study provides a potential guide towards the design of polymer-based photocatalysts.

Experimental

Materials

100 % PET full draw textured yarn filaments with the linear density of 5.4 dtex were employed as the substrate to deposit Ag nanoparticles decorated TiO_2 nanoparticles. All chemicals were of analytical reagent grade and used as received without further purification, including tetrabutyl titanate ($Ti(OC_4H_9)_4$), silver nitrate ($AgNO_3$), sodium hydroxide (NaOH), tert-butanol ($C_4H_{10}O$, TBA), 1,4-benzoquinone ($C_6H_4O_2$, BQ), ethylenediaminetetraacetic acid ($C_{10}H_{16}N_2O_8$, EDTA), anhydrous ethanol (C_2H_6O), methylene blue ($C_{16}H_{18}ClN_3S$,

MB) dye, and methyl orange ($C_{14}H_{14}N_3SO_3Na$, MO) dye. Deionized water was used in all experiments.

Deposition of Ag Nanoparticles Decorated TiO$_2$ Nanoparticles on PET Filament Surfaces

To clean the filaments from any foreign substances as well as improve the bonding strength between the PET substrate and the as-synthesized nanoparticles, the PET filaments were etched in an alkaline solution containing 100 g/*l* NaOH at 100 °C for 45 min with a liquor to goods ratio of 80:1. They were then successively washed with anhydrous ethanol and deionized water at room temperature for 10 min respectively, and finally dried at 80 °C.

A hydrothermal synthetic technique was employed to deposit Ag nanoparticles decorated TiO$_2$ nanoparticles on the surfaces of PET filaments based on our previous study [42]. The schematic of preparation for the Ag nanoparticle-TiO$_2$-PET composites is shown in Scheme 1. Firstly, a series of AgNO$_3$ solutions was prepared by dissolving 0, 0.01, 0.03, 0.05, 0.1, and 0.15 g of AgNO$_3$ in 30 m*l* deionized water (the concentrations of AgNO$_3$ are 0, 0.13, 0.38, 0.63, 1.30, and 1.88 g/*l* in the reaction system), respectively. Six identical TiO$_2$ precursor solutions were also prepared by dissolving 0.6 m*l* of tetrabutyl titanate in 5 m*l* anhydrous ethanol solution, followed by adding 5 m*l* of 95 % ethanol aqueous solution. The TiO$_2$ precursor solutions were evenly mixed with the AgNO$_3$ solutions to obtain six white suspensions under vigorous stirring. Secondly, according to the liquor ratio of 1:80, the same six etched PET filaments were dipped in the above six suspensions, and then transferred to six 100 m*l* Teflon-covered stainless steel autoclaves. 40 m*l* of deionized water was subsequently added in every autoclave, which was put in a reactor for the hydrothermal treatment. Thirdly, the autoclaves were heated to 120 °C at a running speed of 10 r/min. After 3 h, the autoclaves were naturally cooled down to ambient temperature. Lastly, the modified PET filaments were ultrasonically (28 kHz, 100 W) immersed in anhydrous ethanol and deionized water for 10 min thrice based on a liquor ratio of 1:50, respectively.

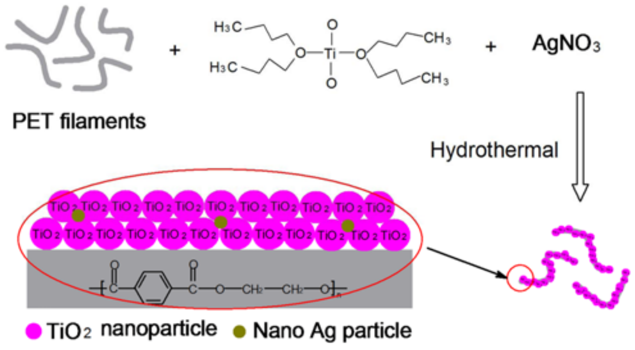

Scheme 1. Schematic of preparation for the Ag nanoparticle-TiO$_2$-PET composites.

Simultaneously, the remaining particles were separated from the suspension by centrifugation, and repeatedly washed with anhydrous ethanol and deionized water, respectively. The as-obtained filaments and particles were dried in a vacuum oven at 80 °C for 12 h. After the hydrothermal treatments, the weight gains were measured to be 1.67±0.02 % for the TiO$_2$ coated PET filaments and 1.65±0.02 % for the Ag nanoparticle decorated TiO$_2$ coated PET filaments.

Characterization Techniques

The Ag (0.63 g/*l* of AgNO$_3$) nanoparticles decorated TiO$_2$ coated PET filaments having the high photocatalytic activity were selected to characterize. The surface morphologies of as-obtained PET filaments before and after treatments were observed by a quanta 450FEG field emission scanning electron microscope (FESEM, FEI Quanta, USA).

The phase compositions of the corresponding as-obtained particles were analyzed by an XRD-7000 X-ray diffractometer (XRD, Shimadzu Corp., Japan) using Cu Kα_1 radiation (λ= 0.154056 nm) at 40 kV and 40 mA at a 2θ range of 10 °-80 °. The crystalline sizes were calculated by using Scherrer equation (1) [43] below:

$$D = K\lambda/\beta\cos\theta \tag{1}$$

where D was the average crystal size, K was the Scherrer coefficient (0.89), λ was the X-ray wavelength (λ=0.154056 nm), θ was the Bragg's angle, β was the width at half-maximum (FWHM) in radians.

The microstructure of the Ag nanoparticles decorated TiO$_2$ nanoparticles was investigated by a JEM-3010 transmission electron microscope (TEM, JEOL Ltd., Japan).

The qualitative and quantitative analysis of the surface elementals and chemical valence states of as-obtained PET filaments were determined by an Axis Ultra X-ray photoelectron spectrometer (XPS, Kratos Analytical Ltd., UK) with the C$_{1s}$ spectrum at 284.8 eV as a standard value. XPS data were acquired using the Al Kα line at 1486.6 eV and a power of 100 W under the vacuum smaller than 10^{-8} Torr condition.

The steady-state photoluminescent (PL) and time-resolved PL spectra were monitored using a FS5 fluorescence spectrophotometer (Edinburgh Instruments Ltd., UK) equipped with a 150 W Xe lamp at an excitation wavelength of 340 nm at ambient temperature. A biexponential function was applied to fit the PL decay spectra based on the following equation (2) [44]:

$$y = A + B_1 e^{(-t/\tau_1)} + B_2 e^{(-t/\tau_2)} \tag{2}$$

where y was the emission intensity at any time t; A was the baseline correction (y-offset); B_1 and B_2 were the constants; τ_1 and τ_2 were the decay times for the exponential components.

The average decay lifetime τ was calculated using the equation (3) [44] below:

$$\tau = \frac{B_1 \tau_1^2 + B_2 \tau_2^2}{B_1 \tau_1 + B_2 \tau_2} \tag{3}$$

The diffuse reflectance spectra (DRS) of as-obtained filaments were recorded on the Lambda 950 spectrophotometer (PerkinElmer Inc., USA) with an integrating sphere (θ=150 mm) using $BaSO_4$ as the reference at a scanning speed of 600 nm/min in 200-800 nm wavebands at ambient temperature.

The valence band characteristics of as-obtained PET filaments were carried out on an Escalab 250 Xi UV ultraviolet photoelectron spectrometer (UPS, Thermo Fisher Scientific Inc., USA). The samples were etched by argon ion before testing.

The electron spin resonance (ESR) measurements were performed on a ESP 300E instrument (Bruker Corporation, Germany) using 5,5-dimethyl-1-pyrrolinen-oxide (DMPO) as the spin trapping reagent for the identification of hydroxyl ($\cdot OH$) in aqueous dispersion and superoxide ($\cdot O_2^-$) in methanol dispersion [45] and 2,2,6,6-tetramethylpiperidine-1-oxyl (TEMPO) [46] for the detection of holes (h^+) in aqueous dispersion at ambient temperature under visible light irradiation. A 150 W Xeon lamp was used as the light source and the visible light (400-780 nm) bandpass filter was applied. The measurement was operated in 9.85 GHz and 19.3 mW with a modulation frequency of 100 kHz and an amplitude modulation of 1.0 Gauss.

Measurements of Photocatalytic Properties

The photocatalytic properties of the as-obtained PET filaments were evaluated by using MB dye and MO dye as the photo-degradation model pollutants under visible light irradiation condition. Typically, 0.3 g of the PET filaments were uniformly dispersed in 60 m*l* of 3 mg/*l* MB solution and placed in the dark for 2 h to achieve an adsorption-desorption equilibrium. Afterwards, the MB solution was exposed to a 30 W Led lamp at a height of 10 cm above the liquid level. The radiation intensity was measured to be 29800 Lux by a TES-1332A digital light meter (TES Electrical Electronic Corp., Taiwan, China). At a specific time t, about 2 m*l* liquor was withdrawn from the dye solution and the absorbance, A_t, of the MB solution was measured at the maximum absorption wavelength of 664 nm using a UV-1600 UV-Vis spectrophotometer (Beijing Beifen-Ruili Analytical Instrument (Group) Co., Ltd., China). The concentration of C_t was calculated according to the standard working curve of MB dye solution (A_t=0.0107+0.1767C_t, R^2=0.99). For MO dye solution, the concentration was calculated by its standard working curve (A_t=-0.0108+ 0.0720C_t, R^2=0.99).

The apparent rate constant k value of dye solution was calculated using the equation (4) [39] below:

$$\ln(C_0/C_t) = kt \tag{4}$$

where C_0 and C_t were the concentrations of dye solution at the initial time and time t.

To identify the reactive radical species in the photocatalytic reaction process, the roles of hydroxyl radicals ($\cdot OH$), superoxide radicals ($\cdot O_2^-$), and holes (h^+) were determined by adding 0.5 m*l* TBA, 1.0 mmol BQ, and 1.0 mmol EDTA quencher in the initial MB solution, respectively [47]. The method was the same as the above photocatalytic experiment.

For the recycle degradation performance, the Ag nanoparticles decorated TiO_2 coated PET filaments were washed with deionized water and redispersed in the fresh MB dye solution under visible light irradiation for 150 min as mentioned above.

To distinguish the effect of the wavelength of monochromatic light on the photocatalytic efficiency of the Ag nanoparticles decorated TiO_2 coated PET filaments, six light sources with the main wavelengths of 420, 470, 520, 590, 620, and 660 nm as well as white light were compared at 350 mA working current for the degradation of MB dye and MO dye solutions at room temperature, respectively. Briefly, 0.05 g of the Ag nanoparticles decorated TiO_2 coated PET filaments, which were cut into short fibers with lengths of 5 mm or so, were suspended in a quartz cuvette containing 30 m*l* of 3 mg/*l* MB solution or 30 m*l* of 5 mg/*l* MO solution. After 2 h of equilibrium duration, the mixture solution was irradiated with different light sources running at a speed of 1000 r/min. The absorbance at λ_{max}=664 for MB or λ_{max}=464 for MO was measured by following the above procedure. Furthermore, the influence of light intensity on the photocatalytic efficiency of the Ag nanoparticles decorated TiO_2 coated PET filaments was assessed by degradation of MB dye solution under white light condition.

Results and Discussion

Surface Morphology of PET Filaments and Structure of As-prepared Nanoparticles

The FESEM images of the etched, TiO_2 coated, and Ag nanoparticle decorated TiO_2 coated PET filaments are shown in Figure 1(a) to 1(e). It is observed that the surfaces of the etched PET filaments are very clear and smooth scattering with a few small pits after being etched with hot alkali solution. When PET filaments are treated with TiO_2 precursor under hydrothermal conditions, the granular substances are homogeneously deposited on the surfaces of both TiO_2 coated and Ag nanoparticle decorated TiO_2 coated PET filaments. The doping of Ag nanoparticles has no obvious influence on the surface morphology of TiO_2 coated PET filaments. Judged from the high-magnified images, these large particles are composed of sub-micrometer sized particles owing to the agglomeration of particles. It is anticipated that the larger specific surface area of PET filaments could be beneficial to adsorb the pollutants and thus could enhance the photocatalytic activity of TiO_2 coated PET filaments [48].

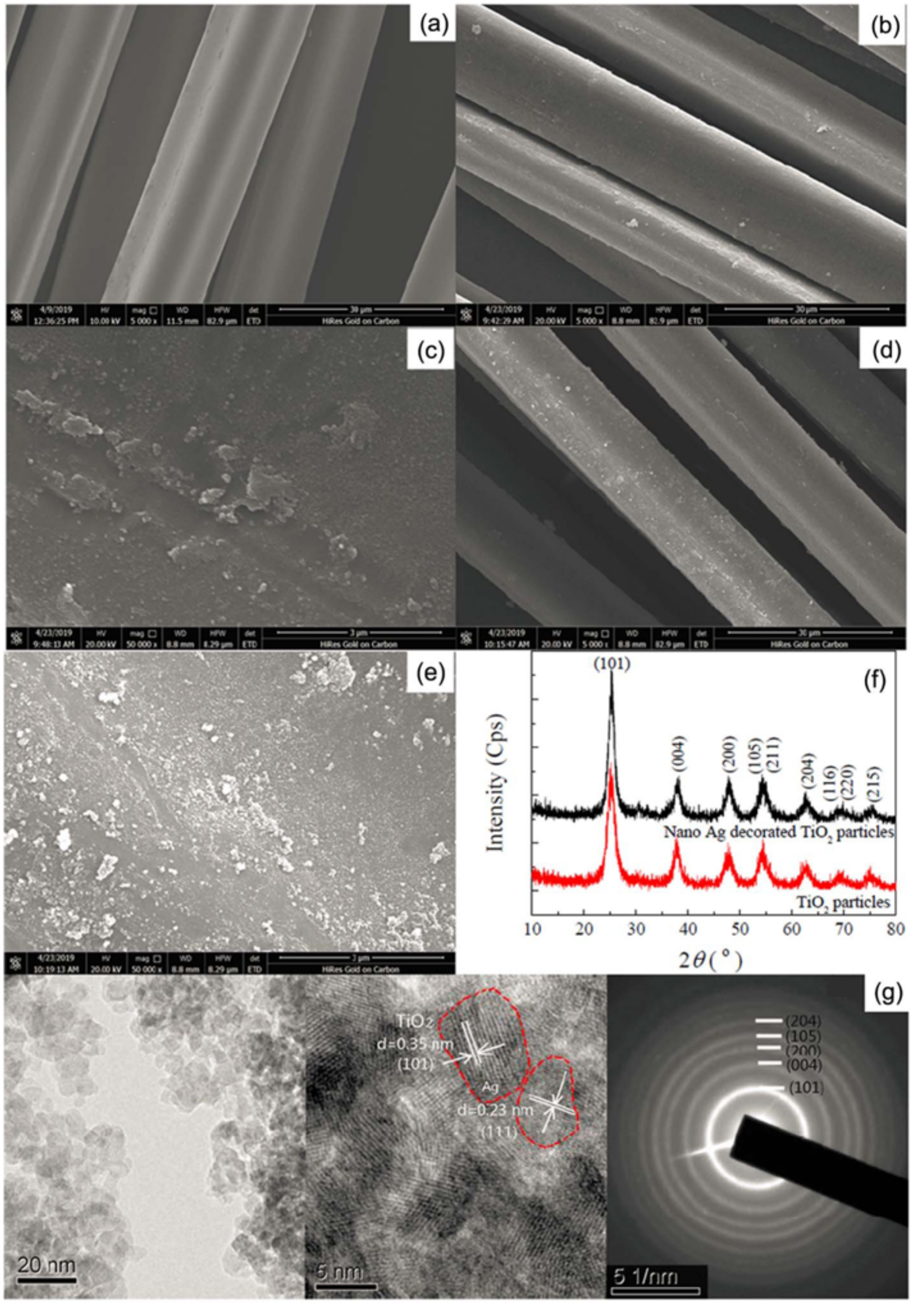

Figure 1. FESEM images of the (a) etched, (b) and (c) TiO$_2$ coated, and (d) and (e) PET filaments coated with Ag decorated TiO$_2$ nanoparticles, (f) XRD patterns of as-obtained TiO$_2$ particles, and (g) TEM, HRTEM and SAED images of the Ag nanoparticles decorated TiO$_2$ nanoparticles.

The XRD patterns of the as-obtained particles are shown in Figure 1(f). All characteristic diffraction peaks appeared at 2θ of 25°, 37°, 48°, 53°, 55° and 62° for both TiO$_2$ particles and Ag nanoparticle decorated TiO$_2$ particles are exactly indexed to the {101}, {004}, {200}, {105}, {211} and {204} planes of anatase TiO$_2$ (JCPDS Card No. 21-1272) [49]. However, the diffraction peaks of metallic Ag are not detected mainly due to its low doping level, high dispersity, and small crystallite sizes. According to the Scherrer's equation, the average crystallite sizes are calculated to be 7.6±0.1 nm for the TiO$_2$ particles and 6.6±0.1 nm for the Ag nanoparticle decorated TiO$_2$ particles. It has been confirmed that the decreased particle size plays a positive role on the photocatalytic activity of the Ag nanoparticle decorated TiO$_2$ particles, leading to the dynamics of electron-hole recombination [50].

The TEM, high-resolution TEM (HRTEM), and selected area electron diffraction (SAED) images of the Ag nanoparticles decorated TiO_2 particles are shown in Figure 1(g). The sphere-like Ag nanoparticles decorated TiO_2 particles are assembled by nano-scaled particles with the particle sizes less than 10 nm. The result is in accord with the particle size measured by XRD analysis. The resolved lattice spacing of the Ag nanoparticles decorated TiO_2 nanoparticles is measured to be 0.35 nm, which is closely matched with the (101) facet of anatase TiO_2 [49]. At the same time, the Ag nanoparticles are found with a fringe spacing of 0.23 nm, which is consistent with the (111) plane of Ag (JCPDS Card No.04-783) [51]. A series of diffraction rings in the SAED pattern are assigned to the (101), (004), (200), (105) and (204) crystal planes of anatase TiO_2 [52].

Chemical Binding States

The XPS analysis was carried out and the full XPS spectra are shown in Figure 2(a). The quantitative XPS data are summarized in Table 1. It is noted that besides the elements of C and O, the element Ti is detected in the TiO_2 coated

Table 1. Results of XPS quantitative analysis of PET filaments

PET filaments	Peak	Binding energy (eV)	FWHM (eV)	Atomic con (%)	Mass con (%)
Etched	C_{1s}	289.61	1.924	78.89	73.72
	O_{1s}	531.56	2.041	21.11	26.28
TiO_2 coated	C_{1s}	286.98	1.924	75.02	67.58
	O_{1s}	531.97	2.134	23.95	28.74
	Ti_{2p}	460.07	1.795	1.02	3.68
Nano Ag decorated TiO_2 coated	C_{1s}	287.20	2.020	81.82	72.38
	O_{1s}	531.75	2.187	16.13	19.01
	Ti_{2p}	459.75	1.795	1.73	6.12
	Ag_{3d}	367.24	1.410	0.31	2.49

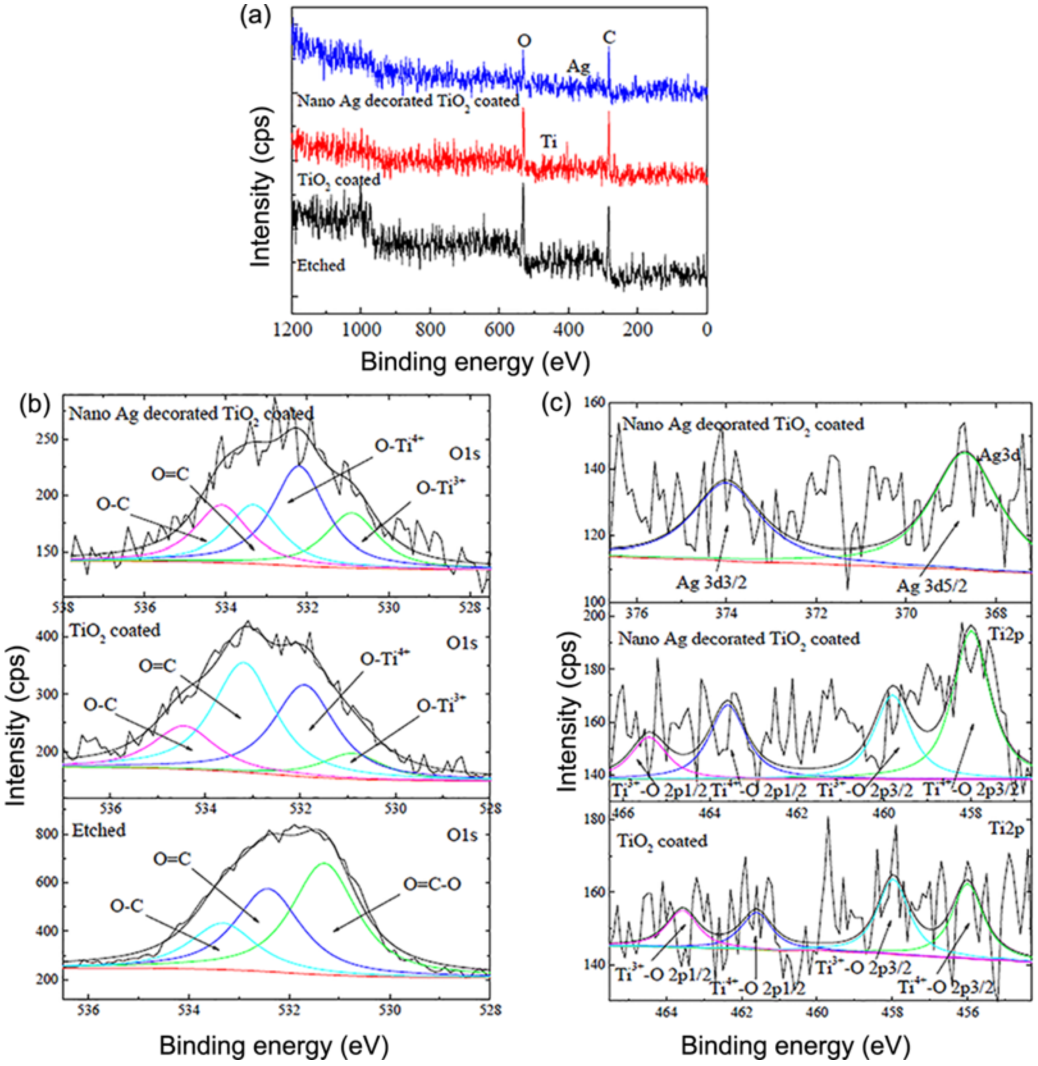

Figure 2. (a) Full XPS spectra of PET filaments, (b) O_{1s}, and (c) Ti_{2p} and Ag_{3d} core-level spectra.

PET filaments. The elements Ti and Ag are observed in the Ag nanoparticles decorated TiO_2 coated PET filaments. The core-level spectra of O, Ti, and Ag are shown in Figure 2(b) and 2(c). The O_{1s} peak of the etched PET filaments is deconvoluted into three sub-peaks centered at 531.3 eV (O=C-O), 532.4 eV (O=C), and 533.3 eV (O-C). After modification with TiO_2 or Ag nanoparticles decorated TiO_2, the binding energy of O=C-O is disappeared. In addition, two new sub-peaks at 530.9 eV (O-Ti^{3+}) and 531.9 eV (O-Ti^{4+}) for the TiO_2 coated filaments and at 530.9 eV (O-Ti^{3+}) and 532.2 eV (O-Ti^{4+}) for the Ag nanoparticles decorated TiO_2 coated filaments are formed, respectively [53]. The corresponding Ti_{2p} peak of the TiO_2 coated filaments is composed of Ti^{4+}-$O_{2p3/2}$ (456.0 eV), Ti^{4+}-$O_{2p1/2}$ (461.6 eV), Ti^{3+}-$O_{2p3/2}$ (458.0 eV), and Ti^{3+}-$O_{2p1/2}$ (463.6 eV) [54]. In the case of the Ag nanoparticles decorated TiO_2 coated filaments, four sub-peaks of Ti^{4+}-$O_{2p3/2}$ (458.0 eV), Ti^{4+}-$O_{2p1/2}$ (463.6 eV), Ti^{3+}-$O_{2p3/2}$ (459.8 eV), and Ti^{3+}-$O_{2p1/2}$ (465.4 eV) are fitted. Compared with the TiO_2 coated filaments, the increases of Ti^{4+}-O and Ti^{3+}-O binding energies of the Ag nanoparticles decorated TiO_2 coated filaments are derived by the interaction of Ag^+ ions with TiO_2 [53]. Furthermore, the Ag_{3d} peak can be deconvoluted into two sub-peaks located at 368.7 eV and 374.0 eV, which are attributed to metallic Ag phase [50]. It has been reported that the photocatalytic activity of the metallic Ag modified titanosilicate photocatalyst is higher than that of the ionic Ag modified ones because silver nanoparticles can be used as the catalyst for oxygen activation [55].

Separation Efficiency of Photo-generated Electron-Hole Pairs

The efficiencies of charge carrier trapping, migration and transfer in the TiO_2 coated and Ag nanoparticles decorated TiO_2 coated PET filaments are studied by the steady-state PL and time-resolved PL spectra, as shown in Figure 3. The intensity of PL spectrum of the Ag nanoparticles decorated TiO_2 coated PET filaments is weaker than that of the TiO_2 coated PET filaments. This implies that the Ag/TiO_2 Schottky junction is formed because of the incorporation of Ag nanoparticles into TiO_2 nanoparticles, which depresses the recombination of electron-hole pairs [56]. It has been verified that the metal ions can be introduced into the lattice of TiO_2 to produce the defect sites [57]. The visible light having a low energy is absorbed by the Ag nanoparticles decorated TiO_2 nanoparticles to excite electron-hole pairs captured at impurity levels, and thus the recombination rate of electrons and holes is significantly inhibited. It has been noted that the photo-oxidation of organic compounds makes a certain contribution to the photocatalytic activity of TiO_2/organic composite photocatalyst [58]. The difference in the electron withdrawing carbonyl functional groups in the molecular structure of PET polymer might change the photoluminescence yield of the primary $n\rightarrow\pi^*$ transition of carbonyl functional groups [59], which could enlarge the degree of delocalized π-bond on the molecular structure of organic compound [60]. In addition, the average fluorescence lifetimes are calculated to be 3.298 ns for the TiO_2 coated PET filaments and 3.347 ns for the Ag nanoparticles decorated TiO_2 coated PET filaments in the time-resolved PL spectra. The longer fluorescence lifetime reveals the prolonged separate rate of electron-hole pairs, which results in the high photocatalytic activity [61]. Therefore, the introduction of Ag nanoparticles into TiO_2 nanoparticles is beneficial for the separation of photogenerated electron-hole pairs. It has been reported that the holes generated from anatase TiO_2 are trapped at the TiO_2 surface within picoseconds, and thereby the trapped holes can survive for nanoseconds, providing sufficient time for oxidation of surface-adsorbed species to take place [27].

Electronic Band Structure

The DRS and UPS spectra of the etched, TiO_2 coated, and Ag nanoparticles decorated TiO_2 coated PET filaments are shown in Figure 4. It is clear from Figure 4(a) that the etched PET filaments possess a strong absorption of UV rays below

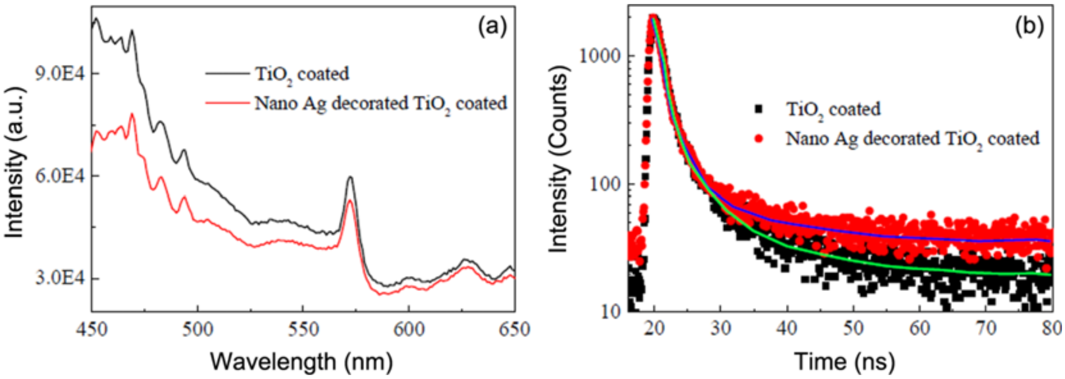

Figure 3. (a) Steady-state PL spectra and (b) time-resolved PL emission decay spectra for the etched, TiO_2 coated, and Ag nanoparticles decorated TiO_2 coated PET filaments.

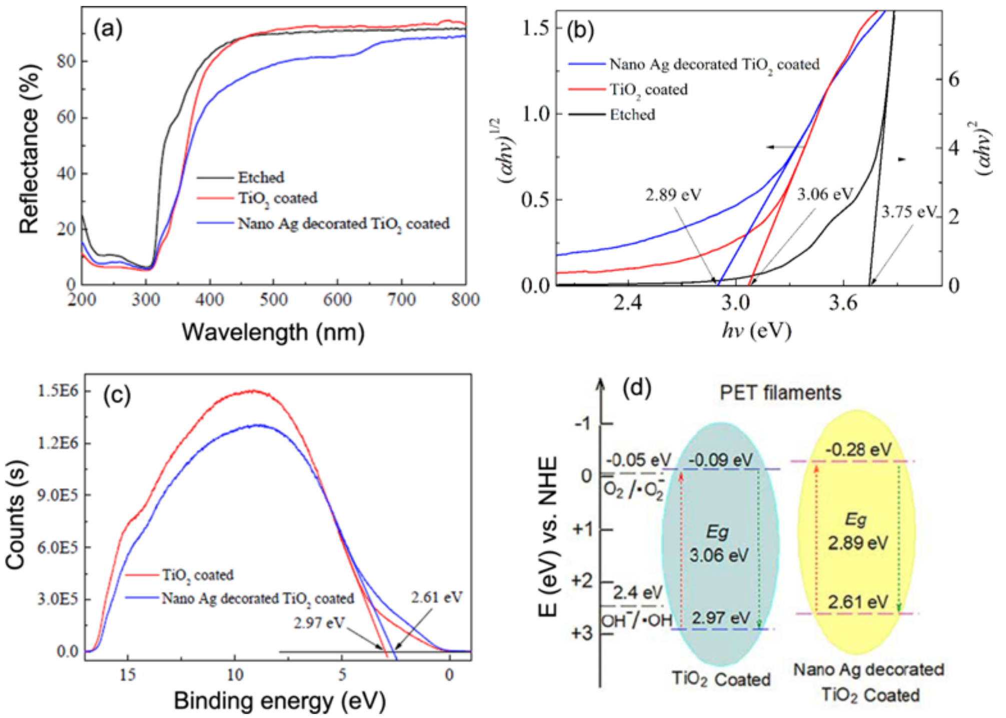

Figure 4. (a) DRS spectra, (b) band gap (E_g) evaluation from the plots of $(\alpha hv)^2$ or $(\alpha hv)^{1/2}$ vs. *hv*, (c) UPS spectra, and (d) comparison of the band gap potentials for the TiO_2 coated and Ag nanoparticles decorated TiO_2 coated PET filaments.

300 nm, which is assigned to the $\pi \rightarrow \pi^*$ electronic transition in the benzene ring [62]. After being coated with TiO_2 nanoparticles, the UV absorption capability of the TiO_2 coated PET filaments is slightly improved along with the red shift of the absorption edge at around 350 nm. This is derived from the electrons excitation of TiO_2 from the valence band to the conduction band. When the Ag nanoparticles are incorporated into TiO_2 nanoparticles, the absorption to UV and especially to visible light of the Ag nanoparticles decorated TiO_2 coated PET filaments are further enhanced. The average reflectance of the Ag nanoparticles decorated TiO_2 coated PET filaments decrease by 11.6 % in visible light waveband as compared with the etched PET filaments. This is primarily caused by the surface plasmon resonance effect of Ag nanoparticles [63].

As illustrated in Figure 4(b), the band gap can be calculated according to the Tauc function: $A(hv\text{-}E_g)^{n/2}=ahv$ [64]. Where E_g is the band gap energy, A is a constant related to the material and the matrix element of the transition, v is the frequency of the incident radiation, h is Planck's constant, α is the absorption coefficient in cm^{-1}, and n depends upon the nature of the transition (n=1 for direct allowed transitions of TiO_2 coated and Ag nanoparticles decorated TiO_2 coated PET filaments, n=4 for indirect allowed transition of etched PET filaments) [65]. The E_g values of the etched, TiO_2 coated, and Ag nanoparticles decorated TiO_2 coated PET filaments are calculated to be 3.75, 3.06, and 2.89 eV by extrapolating the linear part of the $(\alpha hv)^{1/2}$ or $(\alpha hv)^2$ vs. *hv* Tauc plots until their intercepts on the *hv* axis, respectively. So the band gap of the TiO_2 coated PET filaments is narrowed after being incorporated by Ag nanoparticles, which is beneficial for valence band electrons to excite into the conduction band.

The valence band potentials, E_{VB}, are acquired by the UPS spectra of the TiO_2 coated and Ag nanoparticles decorated TiO_2 coated PET filaments, as depicted in Figure 4(c). The intercepts on the binding energy axis in the UPS spectra suggest the valence band energy with respect to the Fermi level [66]. The valence bands are determined to be 2.97 eV for the TiO_2 coated PET filaments and 2.61 eV for the Ag nanoparticles decorated TiO_2 coated PET filaments. The doping of Ag nanoparticles acting as electron sinks results in the appearance of dipole layer, which interferes with band alignment of TiO_2 [8]. Based on the formula $E_g=E_{VB}-E_{CB}$, the conduction band potentials, E_{CB}, are -0.09 and -0.28 eV for the TiO_2 coated and Ag nanoparticles decorated TiO_2 coated PET filaments, respectively. Therefore, the band structures (Figure 4(d)) of the TiO_2 coated and Ag nanoparticles decorated TiO_2 coated PET filaments are determined by using the combination of DRS and UPS.

Photocatalysis Performances

The photocatalytic properties of the Ag nanoparticles decorated TiO_2 coated PET filaments are evaluated by the

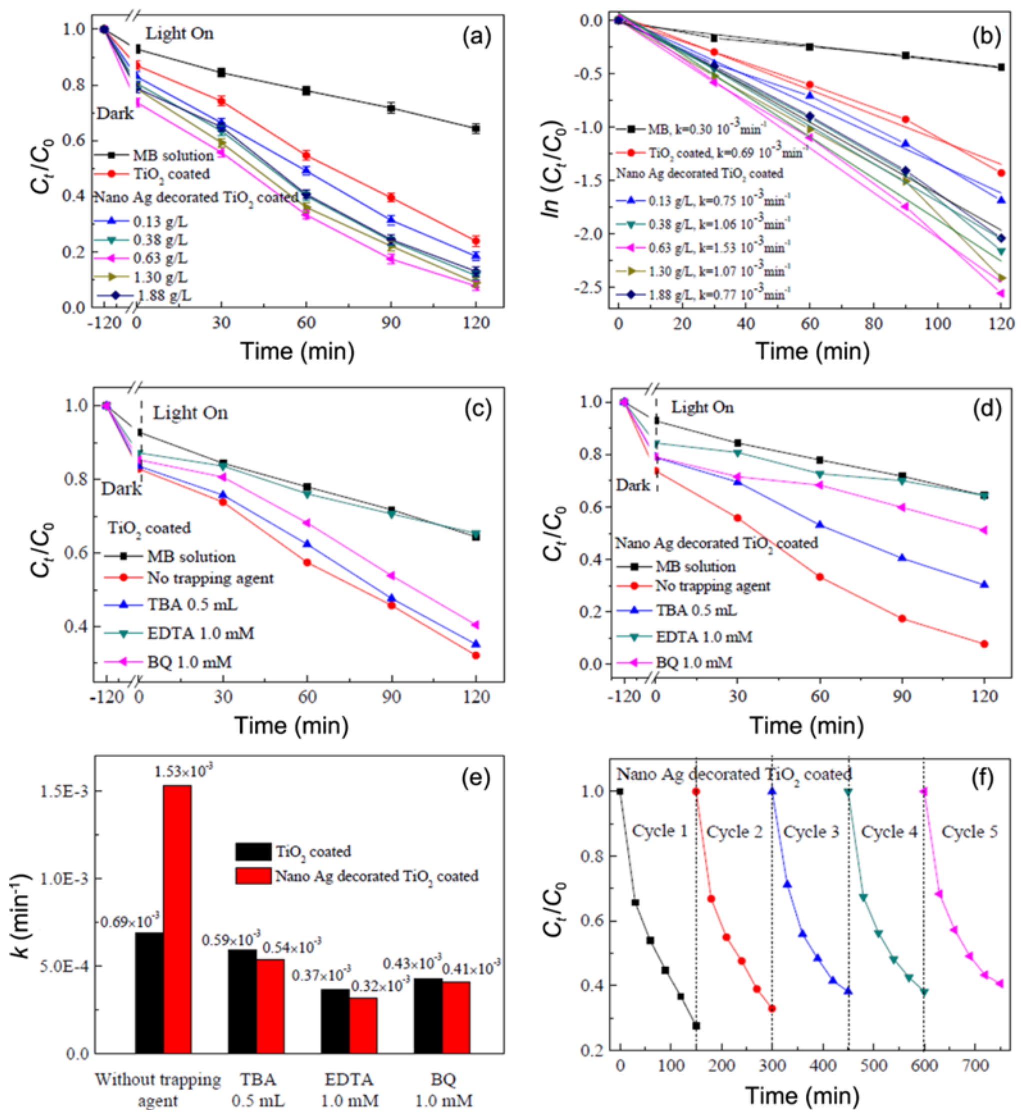

Figure 5. Photodegradation of MB dye and MO dye solutions by the PET filaments coated with Ag decorated TiO_2 nanoparticles under visible light irradiation: (a) effects of the concentrations of $AgNO_3$ on the degradation of MB solution and (b) the corresponding pseudo-first-order kinetic fitting data; trapping experiments for the (c) TiO_2 coated and (d) Ag nanoparticles decorated TiO_2 coated filaments, and (e) comparison of *k* values; (f) cycle degradation of MB solution.

photodegradation of MB or MO dye solution under visible light irradiation, and the results are shown in Figure 5. It is noticed that the photodegradation of the blank MB solution with the apparent rate constant of 0.30×10^{-3} min^{-1} is attributed to the photosensitization reaction of MB dye molecules [67]. The photocatalytic activity of the TiO_2 coated PET filaments are enhanced after being decorated with Ag nanoparticles. The contents of Ag nanoparticles have great influences on the degradation rates of MB solution (Figure 5(a) and 5(b)). As the contents of Ag nanoparticles increase, the apparent rate constant *k* values gradually increase, and reach the maximum of 1.53×10^{-3} min^{-1} when 0.63 g/*l* of $AgNO_3$ is doped with tetrabutyl titanate. Afterwards, the *k* values decrease with the increases of $AgNO_3$. This is because Ag nanoparticles having a suitable plasma resonance band can effectively capture the photogenerated electrons and inhibit the recombination of photo-generated electron-hole pairs, thereby prolonging the lifetime of carriers and improving quantum efficiency [68]. However, the excessive Ag nanoparticles would lead to the decrease of active sites in TiO_2 owing to the space charge repulsion when the concentrations of $AgNO_3$ is beyond 0.63 g/*l*, which results in the formation of new photogenerated electron-hole recombination centers and the increase of the recombination rate [69]. Moreover, the light absorption capability of TiO_2 nanoparticles might be reduced by the

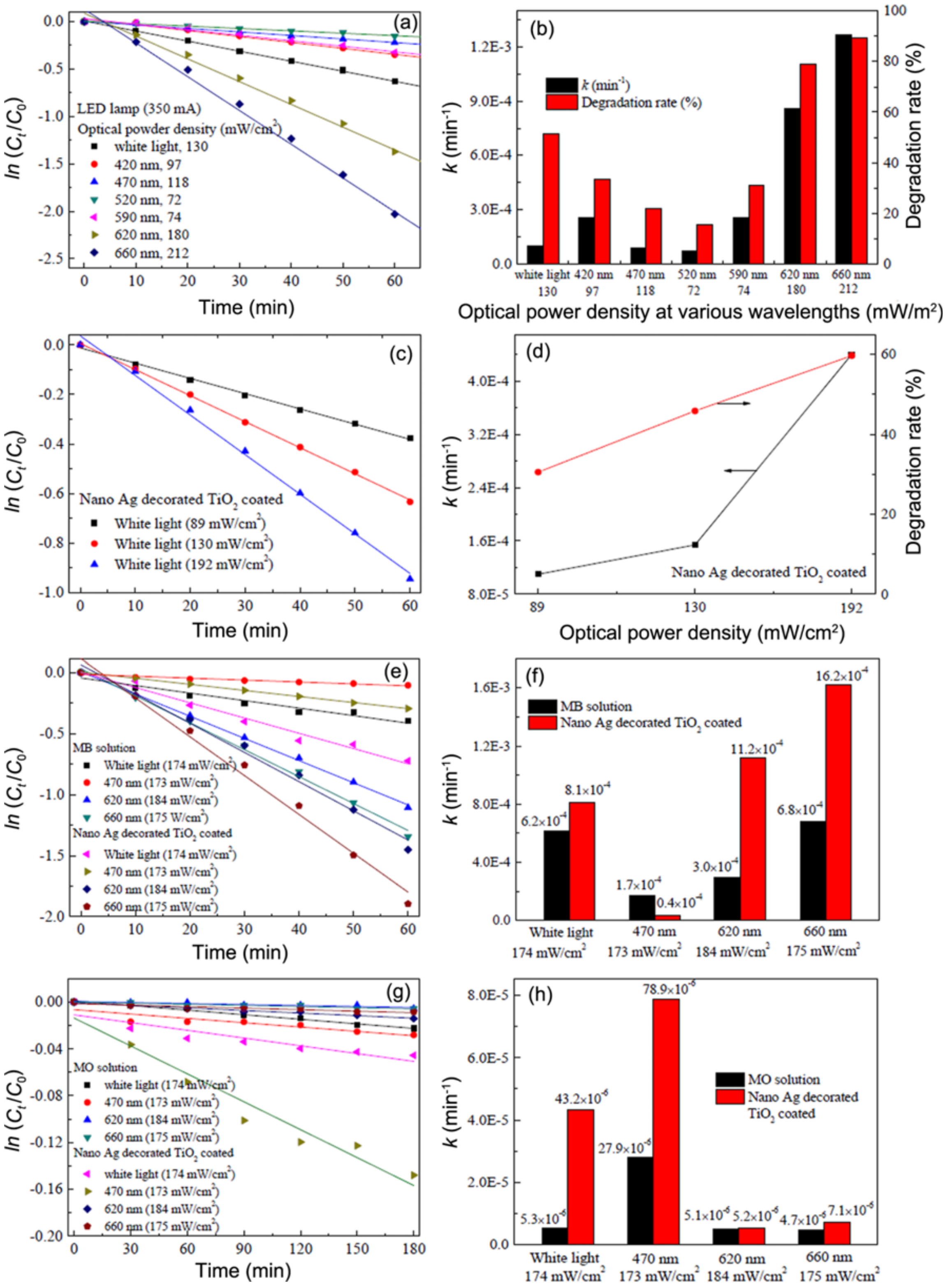

Figure 6. (a) Effects of light wavelengths under 350 mA LED lamp on the degradation of MB solution and (b) comparison of k values; (c) effects of optical power densities for white light on the degradation of MB solution and (d) comparison of k values and degradation rates; effects of various wavelength lights on the degradation of (e) MB dye and (g) MO dye solutions and comparison of k values for (f) MB dye and (h) MO dye solutions under close optical power density conditions.

coating of Ag nanoparticles on the surface of TiO_2 nanoparticles [70].

The reactive radical species involved in the photodegradation of MB are investigated by the trapping experiments (Figure 5(c) and 5(d)). It is clear that when TBA, EDTA, and BQ are applied for the detection of ·OH, h^+, and $\cdot O_2^-$ radicals respectively, the photodegradation of MB dye solution are significantly impaired and the rate constant *k* values are reduced to some degree for the TiO_2 coated and Ag nanoparticles decorated TiO_2 coated PET filaments. The influences of EDTA on the *k* values are more prominent for both filaments in comparison with TBA and BQ (Figure 5(e)). So it is deduced that h^+ is the major active species, while ·OH and $\cdot O_2^-$ play the minor roles in the photodegradation of MB solution. In our previous study [71], it has been demonstrated that the reactive radical species generated by the TiO_2 nanoparticles during the photocatalytic degradation of MB dye solution are mainly ·OH radicals, accompanied by h^+ and $\cdot O_2^-$ radicals. It has also been reported by the trapping experiments that the primary reactive species of the Ag nanoparticle modified anatase TiO_2 are the ·OH radicals [72]. However, when the TiO_2 nanoparticles or Ag nanoparticles decorated TiO_2 nanoparticles are immobilized on PET surfaces, the main reactive species are turned into the holes. This is likely due to the presence of PET polymer substrate, and the reason why the main reactive species change from ·OH radicals into h^+ radicals when PET substrate presences will be investigated in future work.

As shown in Figure 5(f), the consecutive cycles of MB dye photodegradation by the Ag nanoparticles decorated (0.63 g/*l* of $AgNO_3$) TiO_2 coated PET filaments prove that the photocatalytic activity of the Ag nanoparticles decorated TiO_2 coated PET filaments can be maintained to a large extent after five cycles of MB degradation, implying the superior photoactivity of the Ag nanoparticles decorated TiO_2 coated PET filaments.

To further explore the effects of visible light wavelengths, seven LED lamps having monochromatic lights of 420, 470, 520, 590, 620, 660 nm as well as white light (working current 350 mA) are applied for the photodegradation of MB solution. The tested results are shown in Figure 6. It is obvious from Figure 6(a) and Figure 6(b) that the photodegradation of MB solution is influenced by the

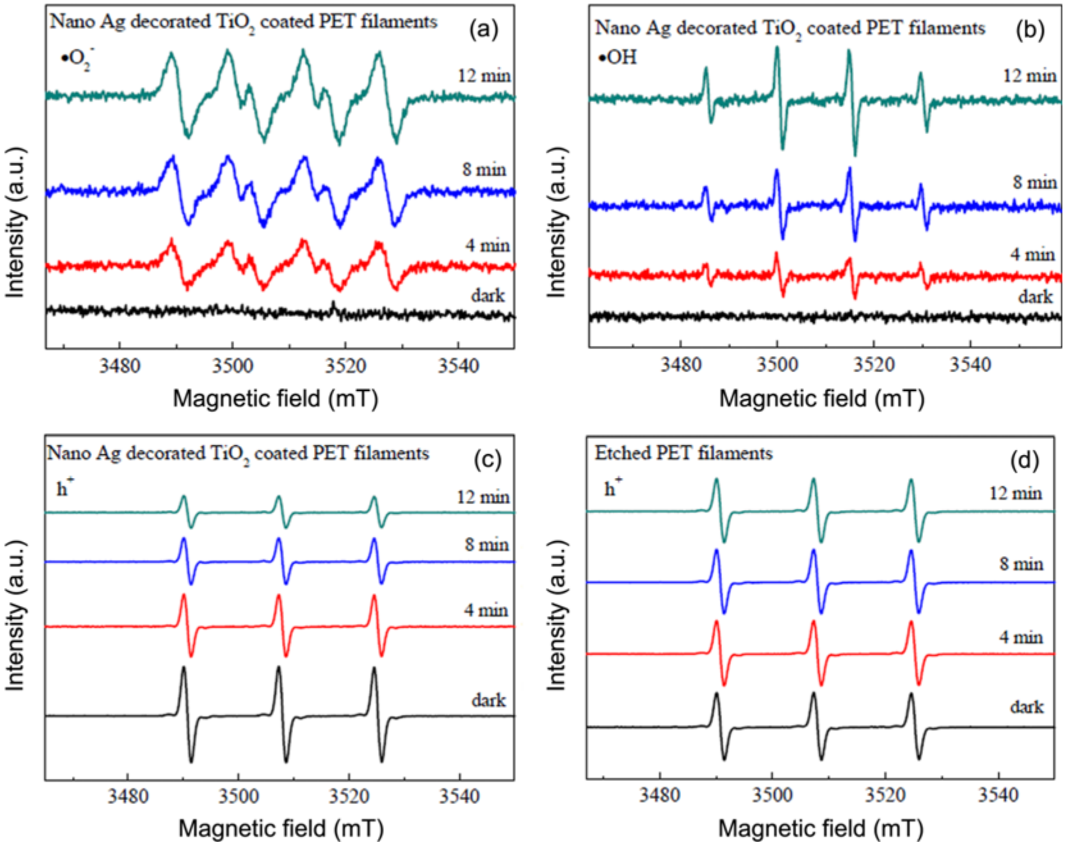

Figure 7. ESR spectra of radical adducts trapped by DMPO for the detection of (a) $\cdot O_2^-$ in methanol dispersion and (b) ·OH in aqueous dispersion for the PET filaments coated with Ag decorated TiO_2 nanoparticles, and by TEMPO for the detection of h^+ in aqueous dispersion for the (c) Ag nanoparticles decorated TiO_2 coated PET and (d) etched PET filaments under visible light irradiation at different times.

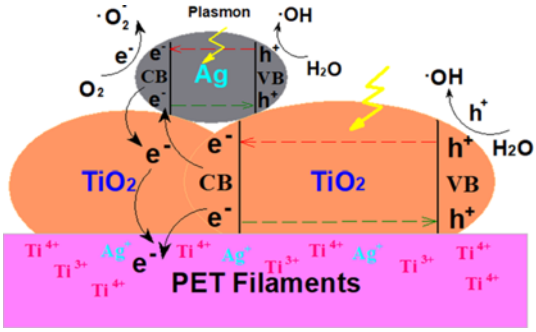

Scheme 2. Proposed photocatalytic mechanism of the PET filaments coated with Ag decorated TiO_2 nanoparticles under visible light irradiation.

wavelength of illumination light, which is consistent with the previous study [41]. The largest *k* value and degradation rate of MB solution by the Ag nanoparticles decorated TiO_2 coated PET filaments can be obtained at the wavelength of 660 nm. Interestingly, we noticed that the optical power densities of various monochromatic lights are different at the same working current of 350 mA. Actually, the photodegradation of MB solution is determined by the optical power density. The larger the optical power density, the larger the *k* values. Thus, the white lights having three optical power densities are used to clarify the effects of optical power density on the degradation of MB solution. It is found that there is a positive correlation between the optical power density and the *k* value or degradation rate (Figure 6(c) and Figure 6(d)). It is demonstrated that the photocatalytic activity of photocatalyst in visible light region depends on the optical spectrum and the position of the onset of absorption band. The photocatalytic activity for polychromatic light appears difficult to rationalize and does not correlate well with crystallographic phases present, and it seems to derive from more complex interplay of different factors [40].

Besides, white light and three monochromatic lights of 470, 620, and 660 nm are applied to illuminate the MB (Figure 6(e) and Figure 6(f)) dye and MO (Figure 6(g) and Figure 6(h)) dye solutions under the close optical power density conditions, respectively. It is evident that the largest *k* values are calculated to be 16.2×10^{-4} min^{-1} at 660 nm for MB solution and 78.9×10^{-6} min^{-1} at 470 nm for MO solution. The matching of the spectrum of light source with the spectrum of target chromophore is very important [73]. As a result, the photodegradation rate of organic dyes is significantly affected by the light wavelength, which is dominantly related to the maximum absorption wavelength of organic dyes. This is because the photodegradation rate of organic dyes is primarily determined by its functional groups, number of carbons, and light adsorption capacity [74]. The presence of electron-withdrawing groups (-COOH, $-SO_3H$, $-NO_2$) or electron-donating groups (-OH, OCH_3, $-NH_2$, $-N(CH_3)_2$, $NH-COCH_3$) can decrease or increase dye degradation [75]. Thus, the environmental applications for photodegradation of organic dyes are specified with specificity and selectivity.

Reactive Radical Species

The scavengers of DMPO and TEMPO are applied to detect the active radical species involved in the MB photodegradation process under visible light irradiation, and the ESR spectra of the Ag nanoparticles decorated TiO_2 coated PET and etched PET filaments are shown in Figure 7. For the Ag nanoparticles decorated TiO_2 coated PET filaments, there are no signals for both DMPO-$\cdot O_2^-$ and DMPO-·OH radical species in dark condition. Upon visible light irradiation, six characteristic peaks for DMPO-$\cdot O_2^-$ (with a 1:1:1:1 intensity ratio for four strong peaks) in methanol dispersion and four characteristic peaks for DMPO-·OH (with a 1:2:2:1 intensity ratio) in aqueous dispersion are observed respectively, and their corresponding signal intensities are gradually enhanced to some extent as the illumination time is prolonged. This indicates that the continuous generation of $\cdot O_2^-$ and ·OH radical species plays a certain role in the degradation of MB dye solution [76]. Meanwhile, the intensity of spin trapped TEMPO-h^+ in dark condition is very strong. As the irradiation time increases, the intensities of spin trapped TEMPO-h^+ decrease gradually under prolonged visible light irradiation, suggesting that the holes make a contribution to the excellent photocatalytic performance of the Ag nanoparticles decorated TiO_2 coated PET filaments [77]. In addition, regarding to the etched PET filaments, the intensities of spin trapped TEMPO-h^+ are not obviously changed regardless of the light source is turned on or off. Thus, the photocatalytic activity is derived from the coating of Ag nanoparticles decorated TiO_2 nanoparticles. By considering the trapping experiments, h^+ is the main active radical species, and $\cdot O_2^-$ and ·OH radical species take part in the photocatalytic reaction too.

Photocatalytic Mechanism

Based on the above results, the underlying photocatalytic mechanism for the Ag nanoparticles decorated TiO_2 coated PET filaments under visible light irradiation is proposed in Scheme 2. Some photoinduced electrons can transfer from TiO_2 nanoparticles to Ag nanoparticles *via* Ti^{3+} states because the Fermi level of TiO_2 is higher than that of Ag, and thereby resulting in the electron capture ability of Ag [78]. At the same time, other photoinduced electrons could migrate from TiO_2 nanoparticles to the substrate of PET as the electronegativity of PET (6.84 eV) is larger than 5.81 eV of TiO_2 according to the Mulliken electronegativity theory [65]. It is reported that the phenolic hydroxyl of kraft lignin has the capability to quench the activity of hydroxyl radicals generated by TiO_2 [79]. It is demonstrated by the XPS analysis that the Ti^{4+}-O/

Ti^{3+}-O bonds are formed *via* the Ti of TiO_2 with the O of benzene rings of PET. The Ti^{4+}/Ti^{3+} cations combined with Ag^+ cations might infiltrate into the amorphous regions of the PET polymers in aqueous solution under high-temperature and high-pressure conditions, which results in the changes of crystallinity, optical and electrical properties of PET polymers. The Ti^{4+}/Ti^{3+} cations and Ag^+ cations doped semiconducting PET polymers might be produced and could trap the photoinduced electrons [80]. Therefore, the PET polymers infiltrated with Ag and Ti not only facilitate the separation of electrons and holes, but also inhibit the recombination of photoinduced charge species, and thus prolong the lifetime and mobility of the charge carriers.

On the other hand, the Ag nanoparticles can absorb the photons *via* the localized SPR excitation under visible light irradiation to generate high energy hot electrons, and these hot electrons can be over the Schottky barrier acting as an electron trapper and transfer from Ag nanoparticles to TiO_2 nanoparticles *via* the intermediate trap states [81], although the Schottky barrier interface hinders the transfer of electron from Ag nanoparticles to TiO_2 nanoparticles [69]. The plasmon-induced interfacial hot-electron transfer has been recently identified by surface enhanced Raman spectroscopy [82]. The hot electrons can migrate across the interfaces between Au (Ag or Cu) and semiconductor (TiO_2 or Cu_2O) at a (sub) nanometer level, and boost the photocatalytic processes [82]. It has been reported that the visible light irradiation can lead to the interfacial charge-transfer transitions between p-conjugated organic molecules and TiO_2 nanoparticles without loss of energy [83]. Thus the photoinduced electrons in TiO_2 might further transfer to the PET substrate infiltrated with Ag and Ti. This process improves the separation efficiency of photoinduced electrons and holes, resulting in the enhanced photocatalytic activity of the Ag nanoparticles decorated TiO_2 coated PET filaments. As a result, most of photoinduced electrons might be trapped by the PET polymers infiltrated with Ag and Ti. It is confirmed that because the dissolved oxygen is a good acceptor of electrons, some of photoinduced electrons can move to TiO_2 surface which further get reduced to $\cdot O_2^-$. Meanwhile, the photoinduced holes can either react with OH^- or H_2O to generate ·OH [19]. The electrons transferred from Ag and TiO_2 nanoparticles to dissolved O_2 are anticipated to be relatively few and slow. A few $\cdot O_2^-$ could be formed, then on protonation yields ·OOH. The OOH radicals and the trapped electrons combine to produce H_2O_2, lastly forming OH radicals. Conversely, the holes on the Ag and TiO_2 nanoparticles are relatively more and react rapidly with OH^- or H_2O molecule to produce ·OH radicals. These ·OH radicals make MB dyes degrade into CO_2 and H_2O. Therefore, combined with the electronic band structure and trapping experiments, the major reactive species are the photoinduced holes for photocatalytic oxidation of MB dyes in visible light region. The hydroxyl and superoxide radicals play a minor role in the photocatalytic reaction.

Conclusion

A coating of Ag nanoparticles decorated TiO_2 nanoparticles, which were chemically grafted *via* O-Ti^{3+}/Ti^{4+} bonds, was deposited on the surfaces of PET filaments by using tetrabutyl titanate as the TiO_2 precursor and silver nitrate as the dopant based on the hydrothermal technique. It was concluded that the separation efficiency of photogenerated electron-hole pairs of Ag nanoparticles decorated TiO_2 nanoparticles was significantly improved because of the narrowed band gap and enhanced light absorption capability under visible light irradiation. The reactive radical species including h^+, $\cdot O_2^-$, and ·OH were involved in the photodegradation process of organic dyes, and h^+ radicals were the major reactive species under visible light irradiation. The enhanced photocatalytic activity of the PET filaments coated with Ag nanoparticles decorated TiO_2 nanoparticles was ascribed to both the incorporation of Ag nanoparticles into TiO_2 nanoparticles and the possible infiltration of Ag/Ti nanoparticles into PET polymers, which could trap the photoinduced electrons and prolong the lifetime and mobility of the charge carriers. Additionally, the photodegradation rate of organic dyes was greatly affected not only by the light intensity but also by the light wavelength. The most efficient wavelength of monochromatic light for photodegradation of organic dyes was correlated with the maximum absorption wavelength of organic dyes.

Acknowledgements

This study has been supported by the National Natural Science Foundation of China (No. 51873169), the International Science and Technology Cooperation Project of Shaanxi Province (2020KW-069), the Sanqin Scholar Foundation (2017), and the Innovation Fund of Postgraduate (No. chx2019003) of Xi'an Polytechnic University.

References

1. F. Y. Ge, Y. M. Chen, A. R. Liu, S. Y. Guang, and Z. S. Cai, *Cellulose,* **26**, 2689 (2019).
2. V. J. Garole, B. C. Choudhary, S. R. Tetgure, D. J. Garole, and A. U. Borse, *Int. J. Environ. Sci. Te.*, **15**, 1649 (2018).
3. W. Zhao, Y. Guo, Y. Faiz, W. T. Yuan, C. Sun, S. M. Wang, Y. H. Deng, Y. Zhuang, Y. Li, X. M. Wang, H. He, and S. G. Yang, *Appl. Catal. B-Environ.,* **163**, 288 (2015).
4. A. Toumazatou, M. K. Arfanis, P. A. Pantazopoulos, A. G. Kontos, P. Falaras, N. Stefanou, and V. Likodimos, *Mater. Lett.,* **197**, 123 (2017).
5. L. J. Liu, Y. Q. Jiang, H. L. Zhao, J. T. Chen, J. L. Cheng, K. S. Yang, and Y. Li, *ACS Catal.*, **6**, 1097 (2016).

6. Y. N. Liu, H. F. Feng, X. B. Yan, J. O. Wang, H. G. Yang, Y. Dua, and W. C. Hao, *Dalton T.*, **46**, 10694 (2017).
7. M. Kwiatkowski, R. Chassagnon, O. Heintz, N. Geoffroy, M. Skompska, and I. Bezverkhyy, *Appl. Catal. B-Environ.,* **204**, 200 (2017).
8. C. Maheu, L. Cardenas, E. Puzenat, P. Afanasiev, and C. Geantet, *Phys. Chem. Chem. Phys.,* **20**, 25629 (2018).
9. H. F. Shi, Y. C. Yu, Y. Zhang, X. J. Feng, X. Y. Zhao, H. Q. Tan, S. U. Khan, Y. G. Li, and E. B. Wang, *Appl. Catal, B-Environ.,* **221**, 280 (2018).
10. M. Amoli-Diva, A. Anvari, and R. Sadighi-Bonabi, *Ceram. Int.,* **45**, 17837 (2019).
11. J. Tripathy, G. Loget, M. Altomare, and P. Schmuki, *J. Nanosci. Nanotechnol.,* **16**, 5353 (2016).
12. O. Kerkez-Kuyumcu, E. Kibar, K. Dayioglu, F. Gedik, A. N. Akin, and S. Ozkara-Aydinoglu, *J. Photochem. Photobiol. A-Chem.,* **311**, 176 (2015).
13. M. J. Li, Z. B. Yu, Q. Liu, L. Sun, and W. Y. Huang, *Chem. Eng. J.,* **286**, 232 (2016).
14. T. Vazhappilly, M. Pilar de Lara-Castells, and D. A. Micha, *Mol. Phys.,* **117**, 2267 (2019).
15. M. Saeed, M. Muneer, M. K. K. Khosa, N. Akram, S. Khalid, M. Adeel, A. Nisar, and S. Sherazi, *Green Process. Synth.,* **8**, 659 (2019).
16. Y. Bai, T. Chen, P. Q. Wang, L. Wang, L. Q. Ye, X. Shi, and W. Bai, *Sol. Energy Mater. Sol. Cells.,* **157**, 406 (2016).
17. J. Wang, X. P. Liang, P. Chen, D. Zhang, S. M. Yang, and Z. F. Liu, *J. Sol-Gel Sci. Technol.,* **82**, 289 (2017).
18. W. J. Liu, W. Han, M. H. Zhang, and Z. Y. Guo, *Polymers,* **11**, 983 (2019).
19. A. Khanna and V. K. Shetty, *Desalin. Water Treat.,* **54**, 744 (2015).
20. C. Cui, Y. W. Qiu, H. H. Hu, N. Ma, S. Li, L. B. Xu, C. R. Li, J. Xu, and W. H. Tang, *RSC Adv.,* **6**, 43697 (2016).
21. K. K. Paul, P. K. Giri, H. Sugimoto, M. Fujii, and B. Choudhury, *Sol. Energy Mater. Sol. Cells,* **201**, 110053 (2019).
22. N. A. Ibrahim, B. M. Eid, E. Abd El-Aziz, T. M. Abou Elmaaty, and S. M. Ramadan, *Int. J. Biol. Macromol.*, **105**, 769 (2017).
23. L. Chen, S. D. Yang, B. Hao, J. M. Ruan, and P. C. Ma, *Appl. Catal. B-Environ.,* **166**, 287 (2015).
24. Y. H. Wang, J. B. Li, C. F. Ding, Y. L. Sun, Y. N. Lin, W. Y. Sun, and C. N. Luo, *J. Photochem. Photobiol. A-Chem.,* **342**, 94 (2017).
25. M. Cieslak, H. Schmidt, K. Twarowska-Schmidt, and I. Kaminska, *Int. J. Environ. Sci. Technol.,* **14**, 1371 (2017).
26. F. Ali, S. B. Khan, T. Kamal, K. A. Alamry, and A. M. Asiri, *Sci. Rep.,* **8**, 6260 (2018).
27. J. Jaksik, P. Tran, V. Galvez, I. Martinez, D. Ortiz, A. Ly, M. McEntee, E. M. Durke, S. T. J. Aishee, M. Cua, A. Touhami, H. J. Moore, and M. J. Uddin, *J. Photochem. Photobiol. A-Chem.,* **365**, 77 (2018).
28. Y. X. Wang, S. Ma, M. N. Huang, H. Yang, Z. L. Xu, and Z. Xu, *Sep. Purif. Technol.,* **227**, 115700 (2019).
29. M. Abid, S. Bouattour, A. M. Ferraria, D. S. Conceicao, A. P. Carapeto, L. F. V. Ferreira, A. M. B. do Rego, M. M. Chehimi, M. R. Vilar, and S. Boufi, *J. Colloid Interface Sci.,* **507**, 83 (2017).
30. D. Kowalczyk, S. Brzezinski, and I. Kaminska, *Text. Res. J.,* **88**, 946 (2017).
31. M. Milosevic, A. Krkobabic, M. Radoicic, Z. Saponjic, T. Radetic, and M. Radetic, *Carbohydr. Polym.,* **158**, 77 (2017).
32. M. Q. Liu, J. Zhao, C. F. Xiao, Q. Quan, and X. F. Li, *Mater. Des.,* **104**, 428 (2016).
33. M. Gorjanc and M. Sala, *Cellulose,* **23**, 2199 (2016).
34. P. M. Dong, X. X. Nie, Z. Jin, Z. F. Huang, X. Y. Wang, and X. W. Zhang, *Ind. Eng. Chem. Res.,* **58**, 7734 (2019).
35. X. M. Zhu, Z. J. Dai, K. L. Xu, Y. Zhao, and Q. F. Ke, *Macromol. Mater. Eng.,* **2019**, 1900350 (2019).
36. Y. Ling, G. Z. Liao, Y. H. Xie, J. Yin, J. Y. Huang, W. H. Feng, and L. S. Li, *J. Photochem. Photobiol. A-Chem.,* **329**, 280 (2016).
37. S. H. Hwang, S. K. Lim, S. H. Hong, S. Kim, W. M. Choi, J. S. Han, and S. H. Lee, *Text. Res. J.,* **86**, 1231 (2016).
38. N. E. Fard and R. Fazaeli, *Russ. J. Phys. Chem. A.,* **92**, 2835 (2018).
39. S. A. A. Vandarkuzhali, N. Pugazhenthiran, R. V. Mangalaraja, P. Sathishkumar, B. Viswanathan, and S. Anandan, *ACS Omega.,* **3**, 9834 (2018).
40. P. Montes-Navajas, M. Serra, A. Corma, and H. Garcia, *Catal. Today,* **225**, 52 (2014).
41. D. L. Kuhn, Z. Zander, A. M. Kulisiewicz, S. M. Debow, C. Haffey, H. Fang, X. T. Kong, Y. Q. Qian, S. D. Walck, A. O. Govorov, Y. Rao, H. L. Dai, and B. G. DeLacy, *J. Phys. Chem. C.,* **123**, 19579 (2019).
42. H. Zhang, F. Li, and H. Zhu, *Fiber. Polym.,* **14**, 43 (2013).
43. H. A. M. Saeed, Y. A. Eltahir, Y. M. Xia, and Y. M. Wang, *J. Text. Inst.,* **106**, 601 (2015).
44. B. Choudhury and A. Choudhury, *J. Lumines.,* **136**, 339 (2013).
45. L. W. Yang, L. L. Liang, L. J. Wang, J. C. Zhu, S. W. Gao, and X. F. Xia, *Appl. Surf. Sci.,* **473**, 527 (2019).
46. F. Chen, Q. Yang, X. M. Li, G. M. Zeng, D. B. Wang, C. G. Niu, J. W. Zhao, H. X. An, T. Xie, and Y. H. Deng, *Appl. Catal. B-Environ.,* **200**, 330 (2017).
47. Y. P. Peng, H. L. Chen, and C. P. Huang, *Appl. Catal. B-Environ.,* **209**, 437 (2017).
48. T. D. Pham and B. K. Lee, *J. Colloid Interface Sci.,* **428**, 24 (2014).
49. Y. Zhang, Z. Y. Zhao, J. R. Chen, L. Cheng, J. Chang, W. C. Sheng, C. Y. Hu, and S. S. Cao, *Appl. Catal. B-Environ.,* **165**, 715 (2015).
50. R. Zhou, S. D. Lin, H. X. Zong, T. T. Huang, F. P. Li, J. H. Pan, and J. Q. Cui, *J. Nanomater.,* **2017**, 4604159 (2017).
51. P. N. Kumar, M. Deepa, and A. K. Srivastava, *Phys. Chem. Chem. Phys.,* **17**, 10040 (2015).

52. L. N. Sun, Z. J. Wang, J. Z. Zhang, J. Feng, J. L. Liu, Y. Zhao, and L. Y. Shi, *RSC Adv.,* **4**, 28481 (2014).
53. K. Lalitha, J. K. Reddy, M. V. P. Sharma, V. D. Kumari, and M. Subrahmanyam, *Int. J. Hydrog. Energy,* **35**, 3991 (2010).
54. A. Kubala-Kukus, D. Banas, I. Stabrawa, K. Szary, D. Sobota, U. Majewska, J. Wudarczyk-Mocko, J. Braziewicz, and M. Pajek, *Acta Pt. B-Atom. Spectr.,* **145**, 43 (2018).
55. Z. X. Ji, M. N. Ismail, D. M. Callahan, E. Pandowo, Z. H. Cai, T. L. Goodrich, K. S. Ziemer, J. Warzywoda, and A. Sacco, *Appl. Catal. B-Environ.,***102**, 323 (2011).
56. H. T. Ren, J. Han, T. T. Li, F. Sun, J. R. Lin, and C. W. Lou, *J. Photochem. Photobiol. A-Chem.,* **377**, 260 (2019).
57. K. K. Mandari, A. K. R. Police, J. Y. Do, M. Kang, and C. Byon, *Int. J. Hydrog. Energy.,* **43**, 2073 (2018).
58. Ali H. Jawad and M. A. Nawi, *J. Polym. Environ.*, **20**, 817 (2012).
59. Ali H. Jawad and M. A. Nawi, *Carbohyd. Polym.*, **90**, 87 (2012).
60. M. A. Nawi, Ali H. Jawad, S. Sabar, and W. S. Wan Ngah, *Carbohyd. Polym.*, **83**, 1146 (2011).
61. S. Qamar, E. C. Lei, L. Liang, S. Gao, K. T. Liu, Y. F. Sun, W. X. Ni, and Y. Xie, *Nano Energy,* **26**, 692 (2016).
62. A. Singh, A. K. Pati, and A. K. Mishra, *Phys. Chem. Chem. Phys.,* **20**, 4167 (2018).
63. Z. Li, A. A. Haidry, Y. S. Liu, L. C. Sun, L. J. Xie, Q. Fatima, and Z. J. Yao, *J. Mater. Sci.-Mater. Electron.,* **29**, 19219 (2018).
64. F. Guayaquil-Sosa, B. Serrano-Rosales, P. J. Valades-Pelayo, and H. de Lasa, *Appl. Catal. B-Environ.,* **211**, 337 (2017).
65. V. A. Zuniga-Ibarra, S. Shaji, B. Krishnan, J. Johny, K. S. Sharma, D. A. Avellaneda, M. J. A. Aguilar, R. T. K. Das, and N. A. Ramos-Delgado, *Appl. Surf. Sci.,* **483**, 156 (2019).
66. S. Samanta, S. Khilari, D. Pradhan, and R. Srivastava, *ACS Sustain. Chem. Eng.,* **5**, 2562 (2017).
67. C. X. Yang, W. P. Dong, G. W. Cui, Y. Q. Zhao, X. F. Shi, X. Y. Xia, B. Tang, and W. L. Wang, *RSC Adv.,* **7**, 23699 (2017).
68. T. T. Shi, X. Y. Hao, J. Y. Ma, H. Liu, G. S. Gai, and Y. H. Zhang, *Mater. Lett.,* **183**, 444 (2016).
69. Y. Zhang, T. Wang, M. Zhou, Y. Wang, and Z. M. Zhang, *Ceram. Int.,* **43**, 3118 (2017).
70. D. Yang, Y. Y. Sun, Z. W. Tong, Y. Tian, Y. B. Li, and Z. Y. Jiang, *J. Phys. Chem. C.,* **119**, 5827 (2015).
71. Q. Tang, H. Zhang, T. Y. Chen, and W. D. Chen, *J. Silk*, **56**, 15 (2019).
72. K. H. Ng, C. H. Lee, M. R. Khan, and C. K. Cheng, *Chem. Eng. J.,* **286**, 282 (2016).
73. J. P. Ghosh, C. H. Langford, and G. Achari, *J. Phys. Chem. A.*, **112**, 10310 (2008).
74. S. Bendjabeur, R. Zouaghi, B. Zouchoune, and T. Sehili, *Spectrochim. Acta A.*, **190**, 494 (2018).
75. S. H. Chen and A. S. Y. Ting, *J. Environ. Manage.*, **150**, 274 (2015).
76. H. J. Liu, P. Chen, X. Y. Yuan, Y. X. Zhang, H. W. Huang, L. A. Wang, and F. Dong, *Chin. J. Catal.,* **40**, 620 (2019).
77. C. Zhang, Y. M. Zhou, Y. W. Zhang, S. Zhao, J. S. Fang, and X. L. Sheng, *Appl. Organomet. Chem.,* **32**, e4160 (2017).
78. W. H. Liu, C. J. Wei, G. D. Wang, X. Cao, Y. X. Tan, and S. Q. Hu, *Ceram. Int.,* **45**, 17884 (2019).
79. M. N. M. Ibrahim, A. Iqbal, C. C. Shen, S. A. Bhawani, and F. Adam, *BMC Chem.,* **13**, 17 (2019).
80. D. T. Scholes, P. Y. Yee, G. R. McKeown, S. Li, H. Kang, J. R. Lindemuth, X. Xia, S. C. King, D. S. Seferos, S. H. Tolbert, and B. J. Schwartz, *Chem. Mater.*, **31**, 73 (2019).
81. G. Sanzone, M. Zimbone, G. Cacciato, F. Ruffino, R. Carles, V. Privitera, and M. G. Grimaldi, *Superlattices Microstruct.,* **123**, 394 (2018).
82. H. Zhang, J. Wei, X. G. Zhang, Y. J. Zhang, P. M. Radjenovica, D. Y. Wu, F. Pan, Z. Q. Tian, and J. F. Li, *CHEM-US,* **6**, 689 (2020).
83. J. I. Fujisawa, R. Muroga, and M. Hanaya, *Phys. Chem. Chem. Phys.,* **17**, 29867 (2015).